



Change in the half-cell open-circuit potential curves of silicon-graphite and nickel-rich lithium nickel manganese cobalt oxide during cycle aging

Julius Schmitt^{a,*}, Markus Schindler^a, Andreas Jossen^{a,b}

^a Technical University of Munich (TUM), Institute for Electrical Energy Storage Technology (EES), Arcisstraße 21, 80333 Munich, Germany

^b Technical University of Munich (TUM), Munich School of Engineering (MSE), Lichtenbergstraße 4a, 85748 Garching, Germany

HIGHLIGHTS

- Half-cell OCP of Si-graphite and NMC-811 is measured at different aging stages.
- Several samples per electrode enable OCP averaging and quantification of deviations.
- The shape of the Si-graphite OCP curve changes during cycle aging.
- Change in Si-graphite OCP is due to reduced contribution of Si to electrode capacity.
- The shape of the NMC-811 OCP curve stays similar during cycle aging.

ARTICLE INFO

Keywords:

Lithium-ion battery
Cycle aging
Half-cell open-circuit potential
silicon-graphite
NMC-811

ABSTRACT

The relationship between the degree of lithiation and open-circuit potential (OCP) of the half-cells of lithium-ion batteries is mostly regarded to be invariant during battery aging. In electrical cell modeling, the OCP curve of aged half-cells is therefore usually obtained by linear scaling of OCP curves measured for pristine electrodes. In this study, the aging invariance of the shape of both half-cell OCP curves of a commercial NMC-811/silicon-graphite cell is investigated experimentally. Full-cells are cycled until different degradation levels are reached. Subsequently, several electrode samples are extracted and the OCP of both electrodes is measured using coin-cells containing electrode samples as working electrode and lithium metal foil as counter electrode. Changes in half-cell OCP are analyzed using differential voltage analysis and incremental capacity analysis. The OCP of the NMC-811 does not change with aging, while the OCP of silicon-graphite exhibits changes which are mainly due to a decrease in the relative capacity contribution of the silicon. The main consequence of our findings is, that changes in the shape of the OCP curve of silicon-graphite during cycle aging should be considered in electrical battery models which are used for full-cell aging diagnostics and state estimation algorithms in battery management systems.

1. Introduction

Degradation processes occurring in lithium-ion batteries during operation and storage result in a reduction of the available energy and power that can be delivered by the battery [1–9]. In addition to this, the degradation also leads to a significant change in the relationship between open-circuit potential (OCP) and state of charge (SOC), which has been the subject of many studies mainly motivated by two aspects: Firstly, monitoring this change can be used as a non-destructive method to investigate the occurrence of different degradation mechanisms [2, 7,8,10–15] and to enable more sophisticated state of health (SOH) estimation [16]. When it is possible to assign degradation to a single

electrode, the SOH can be defined and monitored on the electrode level eventually enabling advanced control algorithms for optimized cell operation [17]. Secondly, knowing the relationship between OCP and SOC with high accuracy during the whole lifetime of a battery is a prerequisite for many methods of state estimation [18–20]. Therefore, a lot of research has been devoted to the development of methods for adjusting the OCP to SOC relationship during battery aging [11,13,21–23].

A common approach reducing the complexity in describing cell aging is to cluster individual aging mechanisms that lead to the same characteristic changes in cell OCP to so called degradation modes [11,13, 14,21,24]. The most important degradation modes are loss of lithium

* Corresponding author.

E-mail address: julius.schmitt@tum.de (J. Schmitt).

<https://doi.org/10.1016/j.jpowsour.2021.230240>

Received 6 April 2021; Received in revised form 2 June 2021; Accepted 1 July 2021

Available online 21 July 2021

0378-7753/© 2021 The Authors. Published by Elsevier B.V. This is an open access article under the CC BY license (<http://creativecommons.org/licenses/by/4.0/>).

inventory (LLI), loss of anode active material (LAM_A) and loss of cathode active material (LAM_C) [11,24]. In a full-cell OCP model consisting of two half-cell OCP curves, LLI results in a shift of the relative position of the anode half-cell curve compared to the cathode half-cell curve [11,24]. LAM is usually treated as a linear scaling of the individual half-cell curves resembling the fact that the individual electrodes can store less lithium but otherwise do not change their properties. The point of the curve which is fixed during this scaling depends on whether degradation occurs while the electrode is lithiated or delithiated [11,24]. This general framework of describing battery degradation via aging modes resulting in a superposition of shifting and linear scaling of half-cell OCP curves has been used in many studies as a tool to extract information on degradation mechanisms from full-cell quasi-stationary OCP curves [2,7,11,13,14,21,24]. It has also been used to simulate the change in OCP during aging [25].

In all of these studies, the shape of the half-cell OCP curves is assumed to be invariant during aging and therefore the aged half-cell OCP is calculated by linear scaling of the pristine half-cell OCP curve. There are only few studies investigating this assumption experimentally: Schmidt et al. showed that the predicted change in full-cell OCP due to LLI and LAM_C can be experimentally validated if these aging modes are artificially evoked during cell preparation [26]. Later, Birkel et al. presented an experimental validation also for the other aging modes using electrode sample manipulation [24].

The effect of cycle aging on the shape of half-cell OCP curves has also been investigated by cycling full-cells and characterizing electrode samples harvested from the aged cells [10,12,27–29]. Only minor deviations in the shape of the OCP curve have been reported for graphite anodes [10,12]. However, much larger alterations of the OCP curve shape have been found for blend anodes consisting of graphite and silicon. These alterations of the curve shape are associated with a faster degradation of the silicon in comparison to the graphite [27–29]. Anseán et al. recently presented a method to construct the OCP of blended silicon–graphite (SiG) electrodes based on the OCP curves of their components [30].

There are only few studies where a change in the shape of the NMC OCP curve during full-cell cycling is investigated experimentally [29,31–33]. Lee et al. presented an algorithm to extract the half-cell OCP curves from full-cell low-current charging data and showed that adapting the shape of the cathode OCP curve for aged cells leads to an improvement in the accuracy of the full-cell OCP which they reconstructed from the half-cell OCP curves [22].

The aim of this study is to experimentally investigate changes in the shape of the electrode OCP curves of blended silicon–graphite anodes and NMC-811 cathodes during cycle aging. We therefore cycle commercial cylindrical cells containing these electrode materials and open them at different aging stages to harvest electrode samples. By cycling the electrodes in the full-cell configuration, we ensure that the electrode degradation occurs in a setting similar to an application. We finally measure the half-cell OCP of the harvested samples in coin-cell configuration vs. lithium metal foil.

Our work is distinguished to former studies in two aspects: Firstly, we perform electrode characterization at multiple aging stages allowing an analysis of the change in half-cell OCP as a function of full-cell charge throughput, i.e., number of equivalent full cycles in full-cell configuration. Secondly, we base our results on measurements of several electrode samples taken from one electrode. This allows us to give an estimation of the accuracy of the method, reduces the influence of uncontrollable processes during sample extraction and coin-cell manufacturing, and provides a possibility to take into account spatial inhomogeneity of the electrodes [34,35].

2. Experimental

2.1. Investigated cells

In this study, commercially available cylindrical cells of the type INR18650-MJ1 from LG Chem were investigated. The cells have a nominal minimum capacity of 3.35 Ah according to the manufacturer. C-rates used to operate full-cells are always given with respect to this capacity in this work. Sturm et al. showed that the cathode of this high-energy cells is based on nickel-rich NMC-811 while the anode is based on a combination of graphite and silicon with a silicon fraction of ca. 3.5 wt.% [36]. Based on the dimensions of the double-side coated electrodes of this cell, which are 5.8×61.5 cm [36], the nominal areal capacity of the electrodes corresponds to 4.7 mAh/cm^2 per side. This cell type was chosen for this study because it contains state-of-the-art electrode materials and the process for extracting electrode samples and manufacturing coin-cells using electrode material from this cell type has been optimized previously at our institute [36].

2.2. Cycle aging and electrochemical characterization of cylindrical full-cells

After delivery, all cells were initially tested according to a series of procedures, internally standardized at our institute [37–39]. This standardized initial characterization is conducted to gain information on the long-term development of cell parameters of this type of commercial cells [37]. Eight cells were randomly chosen for the experiments which are presented in this study. They are referred to as cell #1–8.

A schematic overview of the experimental procedure excluding the initial characterization is shown in Fig. 1(a). An HRT-M10 battery test system from Battery Dynamics (Germany) was used for characterizing and cycling the full-cells. The cells were kept at 25°C inside an MK53 climatic chamber from BINDER (Germany) during the experiments. The voltage limits recommended by the cell manufacturer, i.e., $U_{\min} = 2.5 \text{ V}$ and $U_{\max} = 4.2 \text{ V}$, were used for all tests. First, a capacity checkup consisting of two CCCV cycles ($I_{\text{dch}} = 0.2 \text{ C}$, $I_{\text{ch}} = 0.5 \text{ C}$, $I_{\text{cutoff}} = 50 \text{ mA}$ for both charging and discharging) was conducted. Then, a low-current CCCV cycle to determine the quasi-stationary OCP was applied. The current for both charging and discharging was set to 0.033 C , the cut-off current was 0.001 C and a 6 h pause followed each CV phase. Cells #2–8 were then cycled for up to 550 cycles consisting of 1 C CC discharge and 0.5 C CCCV charge steps with $I_{\text{cutoff}} = 0.03 \text{ C}$. A pause of 30 min duration followed each discharge and charge step. The cycling was terminated after a different number of cycles for each cell (see Table 1) in order to have cells at different aging stages for the following characterization procedures and the subsequent electrode sample extraction. The individual number of cycles was defined for each cell at the beginning of the cycling period and was not influenced by the aging progress an individual cell exhibited during the cycling period.

After the cycling, another quasi-stationary OCP measurement and a galvanostatic titration technique (GITT) measurement were conducted. For cells #2, 3, and 4 there was an additional capacity checkup before the quasi-stationary OCP measurement after the cycling period, which was not applied to the other cells. Finally, the cells were CCCV discharged to 3 V with 0.5 C and $I_{\text{cutoff}} = 0.115 \text{ C}$ and then opened.

Cell #1 was used as a reference in this study. After the initial characterization described in [37], it was subject to five CC cycles and two CCCV cycles according to the specifications presented in [37]. It was then characterized using the same procedures as the other cells (capacity checkup, quasi-stationary OCP measurement, GITT). Subsequently, it was discharged and opened without any further cycling.

The total charge throughput until the opening of the cells Q_{opening} is used as a measure for the aging stress applied to the cells. It is given in equivalent full cycles (EFC) with one EFC corresponding to a charge throughput of twice the nominal capacity, equivalent to

Table 1

Overview of parameters of the investigated cells. Cycles corresponds to the number of nominal cycles applied during the cycling period. For cell #1 only one quasi-stationary OCP measurement was conducted in full-cell configuration, therefore C_{EOL} is equal to C_{BOL} .

Cell #	Cycles	$Q_{opening}/EFC$	C_{BOL}/Ah	C_{EOL}/Ah	$SOH_{EOL}/\%$
1	0	11.2	3.4139	3.4139	100
2	50	56.0	3.4715	3.3636	96.9
3	100	103.1	3.4809	3.3218	95.4
4	200	195.4	3.4815	3.2556	93.5
5	400	363.1	3.4856	3.0704	88.1
6	450	411.4	3.4936	3.1139	89.1
7	500	445.5	3.4913	3.0602	87.7
8	550	487.5	3.4885	2.9974	85.9

charging and discharging the cell by the nominal capacity. For the cell under investigation with a nominal capacity of 3.35 Ah, this means that one EFC equals 6.7 Ah. The charge throughput during the standard initial characterization is excluded for the calculation of $Q_{opening}$.

2.3. Cell opening and manufacturing of coin-cells

After being discharged to 3 V, the cells were opened inside an Argon-filled glove box (M. Braun Inertgas-Systeme, Germany). The electrodes were partially unrolled and the section between 6 cm and 18 cm measured from the beginning of the double-side coated area at the outer end of the electrode jelly-roll was cut out. A schematic side view and a top view of a harvested silicon-graphite electrode are shown in Figs. 1(b) and 1(c) to illustrate the position on the jelly-roll where the samples were extracted. The same position was chosen for sample extraction on the cathode but with the difference that there was no single-coated area at the outer end of the jelly-roll. The electrode sections were then fixed on a glass plate using adhesive tape as suggested in the literature [40] with the originally inward facing side (in the rolled up configuration) now being on top. The coating on the side now facing the top was removed by both mechanical abrasion using a scalpel and applying a solvent. Diethyl carbonate (DEC, 99 %, Merck) was used as solvent to remove anode coating while N-methyl-2-pyrrolidone (NMP, 99.5%, Sigma-Aldrich) was used to remove the cathode coating. Subsequently, six circular samples with 14 mm diameter were punched from the middle of the electrode section.

Half-cells in the CR2032 coin-cell format with lithium metal foil as anode were built with the SiG samples under Argon atmosphere following the procedure presented in [36]. Inside the housing the cells contained a stack consisting of a 0.5 mm aluminum spacer, a circular piece of lithium metal foil (15.6 mm diameter, 250 μ m thickness), two glass fiber separators (16 mm diameter, 260 μ m thickness each, VWR, type 691) filled with 90 μ l of 1 M LiPF₆ in 3:7 (wt:wt) ethylene carbonate (EC)/ethyl methyl carbonate (EMC) electrolyte (LP57, 99.9%, Solvionic, France), a SiG sample, a 1 mm aluminum spacer, and a spring. A schematic of the coin-cell stack is shown in Fig. 1(d).

The cathode samples were wetted under vacuum in a pressure chamber (Harro Höflinger Verpackungsmaschinen, Germany) within the glove box as suggested by Sturm et al. [36] in order to properly fill the low porous electrode with electrolyte. The pressure profile shown in Table 2 was used for the wetting process. Afterwards, half-cells in coin-cell format were built with the cathode samples following the same procedure as for the anode samples with the exception that only 70 μ l of LP57 were added.

2.4. Characterization of coin-cells

The coin-cells were put into a climatic chamber at 25 °C and connected to a CTS battery test system from Basytec (Germany). First, the cells were kept at open-circuit conditions for 12 h to allow the electrolyte to fully soak into the separator disks and electrode samples.

Afterwards, the quasi-stationary OCP was obtained by cycling the coin-cells at low-current rates. First, the cells were discharged (lithiation of the harvested electrode sample) with a current of 160 μ A until the lower cut-off voltage was reached. Afterwards, they were fully charged (delithiation of the harvested sample) with a current of 80 μ A until the upper cut-off voltage was reached and subsequently fully discharged with a current of 80 μ A until the lower cut-off voltage was reached again. The last two steps were repeated once to have two full cycles in total after the initial discharge step. Based on the nominal areal capacity and the electrode sample area of 1.54 cm², the coin-cell capacity is estimated to be 7.2 mAh. The current therefore corresponds to a current rate of approximately C/90. The coin-cells containing NMC-811 were cycled between 3.0 V and 4.3 V, the coin-cells containing SiG between 0.01 V and 1.7 V. Due to a technical problem, the half-cell measurements with the samples taken from cell #4 were not carried out correctly. These measurements are therefore excluded from the analysis.

3. Results and discussion

3.1. Full-cell degradation during cycling

In Table 1 an overview on the parameters of the individual full-cells is given including the total charge throughput $Q_{opening}$ the cells have experienced until they were opened. The capacity measured during the quasi-stationary OCP measurement (CCCV discharging) conducted at begin of life (BOL) C_{BOL} is also listed in Table 1. C_{BOL} of cell #1 is slightly smaller than the mean C_{BOL} of the other cells although it comes from the same production batch. This is probably due to two reasons: Firstly, the cell experienced some additional cycling compared to the other cells corresponding to 6.9 equivalent full cycles before the characterization was conducted. Secondly, the tests with cell #1 were conducted 205 days after the beginning of the tests with the other cells. Therefore, there might be some additional calendar aging affecting cell #1 even though it was stored at 4 °C during this time.

The capacity of cells #2 to 8 decreases during the cycling period as depicted in Fig. 2 where the CC discharge capacity extracted during the single cycles is plotted as a function of the charge throughput during cycling $C_{cycling}$. The rate of capacity decrease does not stay constant for the individual cells during the whole cycling period but changes during aging even though the experimental conditions stay the same. Despite the fact that the cells show no significant difference in capacity at BOL and are exposed to the same aging conditions, their capacities exhibit an increasing spread during aging as the individual cell capacities decrease at different rates. Production related differences inside the cells leading to an intrinsic difference in their aging behavior are the most probable reason for this. Production related differences in the calendar aging rate have been reported for this cell type before [38].

The SOH of the cells determined during the quasi-stationary OCP measurement at the end of life (EOL) just prior to the cell opening is lower for cells that have been cycled for a larger number of cycles as depicted in Table 1. The SOH is here defined as the ratio between the CCCV discharge capacity during the quasi-stationary OCP measurement after the cycling period C_{EOL} (also shown in Table 1) and the CCCV discharge capacity during the quasi-stationary OCP measurement before the cycling period C_{BOL} . The only exception to this trend is cell #5 which has a lower SOH at EOL than cell #6 even though it experienced less cycling. As discussed before, this is probably due to production related differences in the cells leading to different individual aging behavior. Despite these differences in individual aging behavior, the differences in SOH after the cycling period show that the cells are aged to different degrees at the point of cell opening. Therefore the electrodes should also be in different aging states, thus allowing an analysis of the influence of cycle aging on the open-circuit potential curve of the electrodes.

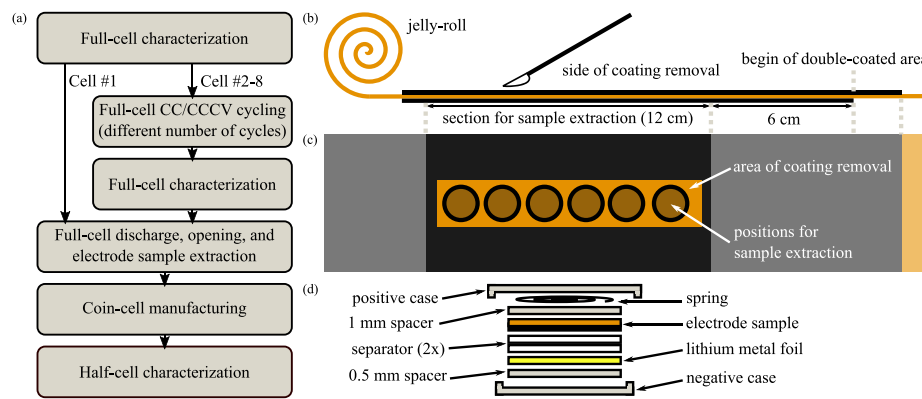


Fig. 1. (a) Overview on the experimental procedure. (b) Schematic side view of a harvested silicon-graphite electrode. (c) Schematic top view of a harvested silicon-graphite electrode. (d) Schematic side view of a coin-cell stack.

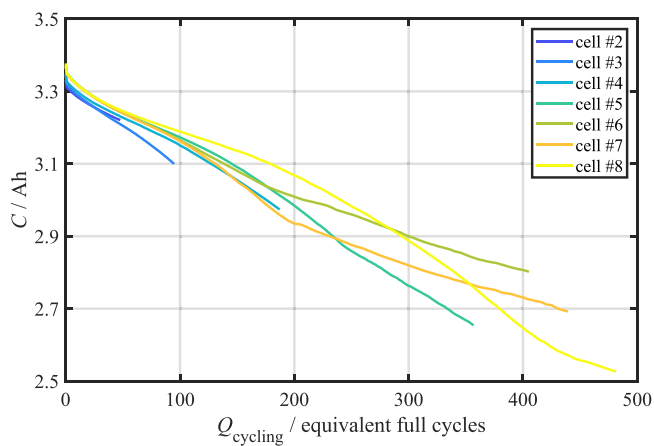


Fig. 2. Development of the full-cell discharge capacity during the cycling period (1 C CC discharging and 0.5 C CCCV charging at 25 °C) as function of the charge throughput during the cycling period.

Table 2
Pressure profile used for wetting the cathode samples.

Step	Pressure/mbar	Duration/s
Vacuum I	12	10
Release I	60	10
Vacuum II	22	20
Release II	80	10
Vacuum III	32	10
Wetting	32	1

3.2. Reproducibility of half-cell open-circuit potential measurements using coin-cells

The quasi-stationary OCP curves obtained from several coin-cells built with material from the same electrode exhibit certain differences between each other. There are probably two main reasons for these differences. Firstly, it might be possible that the electrode is inhomogeneous [35] to some degree and therefore the individual samples taken from one electrode also differ to some degree. Secondly, the manual handling steps during sample extraction and coin-cell preparation could introduce small differences between the individual coin-cells even if all steps were carried out with high thoroughness.

A quantitative measure for the differences between the OCP curves obtained from the coin-cells built from one electrode can be defined as the mean standard deviation over the whole SOC range σ_{OCP} , which is

calculated according to

$$\sigma_{\text{OCP}} = \frac{1}{N_{\text{step}}} \cdot \sum_{i=1}^{N_{\text{step}}} \sqrt{\frac{1}{N_{\text{coin}} - 1} \sum_{j=1}^{N_{\text{coin}}} (U_{ij} - \bar{U}_i)^2} \quad (1)$$

where N_{step} is the number of equally spaced points of the SOC range at which the measured curves are interpolated for comparison (here $N_{\text{step}} = 2800$), N_{coin} is the number of working coin-cells built from one electrode of the full-cell, U_{ij} is the quasi-stationary OCP of the j th coin-cell at the i th SOC interpolation point and \bar{U}_i is the arithmetic mean of the OCP at the i th SOC interpolation point of the coin-cells built from the same electrode. In Table 3 σ_{OCP} is listed for all sets of coin-cells for the first and second low-current charging and discharging step. The sets of coin-cells used for this analysis consist of different numbers of coin-cells, which are also listed in Table 3, because some of the coin-cells did not work properly and were therefore excluded.

The mean σ_{OCP} is lower for the first quasi-stationary cycle iteration for both electrode types and current directions as indicated in Table 3. The shape of the quasi-stationary OCP obtained during the first and the second low-current cycle is similar for most coin-cells. We draw the conclusion that the first cycle is better suited to analyze the change in electrode OCP due to the following reasons: Firstly, the influence of additional degradation in the coin-cell configuration during the OCP measurement, which takes approximately eight days per cycle, is minimized. Secondly, the lower mean σ_{OCP} obtained during the first cycle indicates a higher reproducibility of the results. Therefore, we use only the OCP curves obtained during the first low-current cycle applied to the coin-cells for the further analysis in the scope of this study. Besides that, we want to emphasize that the σ_{OCP} values shown in Table 3 do not exhibit a trend during the progress of the full-cell cycling which shows that our method is suitable to measure the half-cell OCP of both pristine and aged cells.

For the analysis of the change in the shape of the electrode OCP curves, averaged quasi-stationary OCP curves are used in the following sections. For the averaging, the quasi-stationary OCP curves measured for the individual coin-cells built from one electrode are linearly interpolated at 2800 equally spaced SOC points and the arithmetic mean of all curves is treated as the averaged OCP at this SOC. The aim of this averaging is to reduce the influence of non-controllable, statistical variations induced by the manual coin-cell manufacturing and thereby enhancing the reproducibility of the averaged results. In addition to that, by using averaged OCP curves, possible inhomogeneity in radial direction of the jelly-roll is considered at least to some extent and therefore the averaged results might resemble the actual situation in a large size electrode better than just looking at the results obtained from one comparably small fraction of the electrode. Contrariwise, it has to be stated that due to the averaging, the sharpness of voltage steps observed in the curve is reduced but which might actually resemble the OCP curve of an inhomogeneous electrode [35].

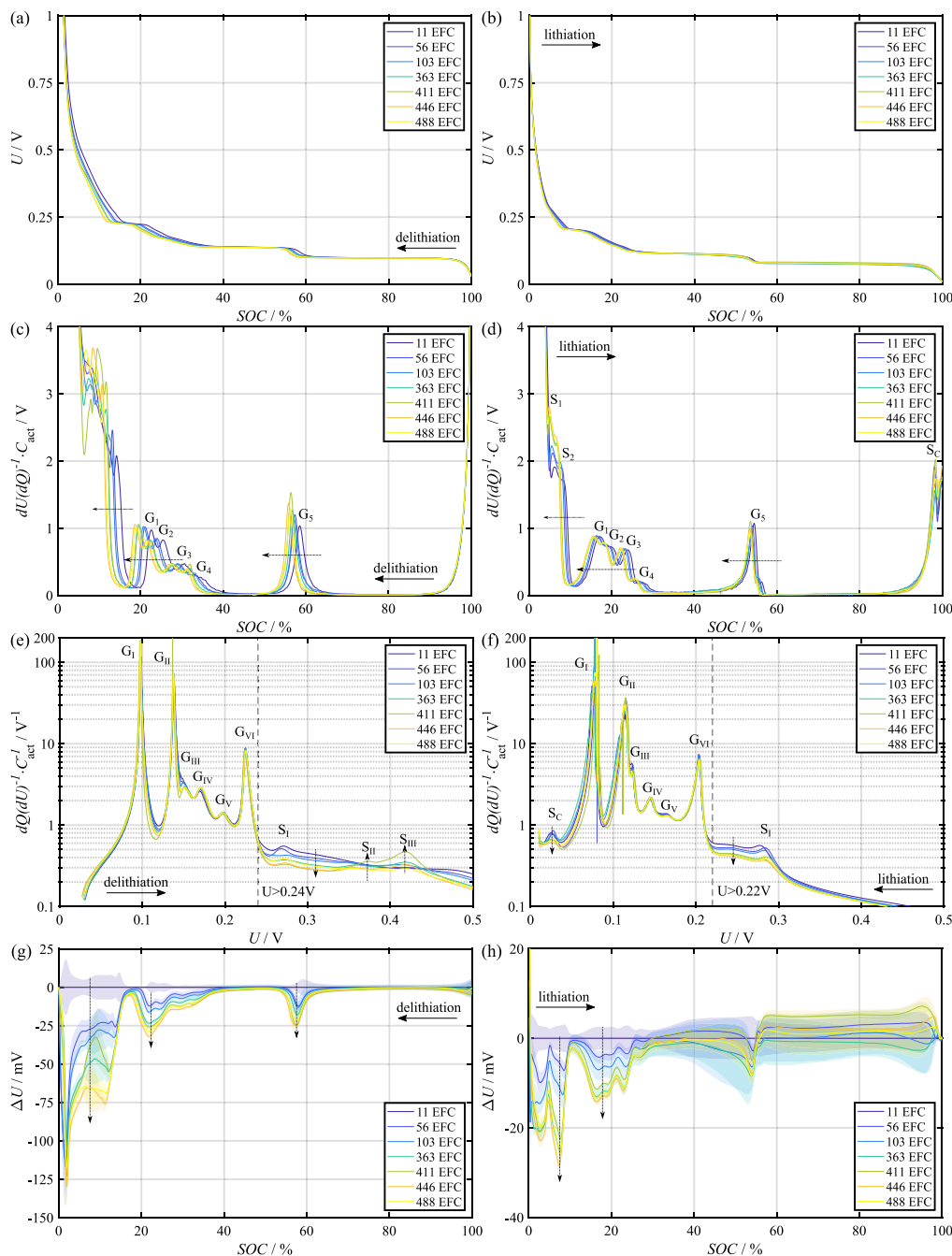


Fig. 3. First row: Mean quasi-stationary OCP vs. Li/Li^+ during (a) delithiation and (b) lithiation of the silicon-graphite samples extracted from full-cells that have been cycled for the number of equivalent full cycles indicated in the legend. Second row: Differential voltage during (c) delithiation and (d) lithiation of the silicon-graphite samples calculated based on the averaged OCP curves. The differential voltage values are normalized by multiplying with the actual capacity during the respective (dis-)charging step C_{act} and smoothed using a moving average filter. Third row: Incremental capacity during (e) delithiation and (f) lithiation of the silicon-graphite samples calculated based on the averaged OCP curves and plotted against cell voltage vs. Li/Li^+ . The incremental capacity values are normalized by multiplying with the inverse of the actual capacity during the respective (dis-)charging step C_{act} and smoothed using a moving average filter. Fourth row: Difference between mean OCP of aged silicon-graphite samples and mean OCP of pristine silicon-graphite samples during (g) delithiation and (h) lithiation. The standard deviation between the OCP of the single samples harvested from the same electrode is shown as shaded area.

3.3. Change in the silicon-graphite delithiation open-circuit potential curve during cycle aging

In Figs. 3(a) and 3(b) the mean voltage curves obtained during the first delithiation and lithiation step applied to the coin-cells containing SiG samples from full-cells at different aging stages are displayed. The electrode SOC plotted on the x -axis is based on the actual coin-cell capacity at the respective aging stage. The shape of the voltage curves and their change is analyzed using differential voltage analysis

(DVA), which is commonly used to identify phase transitions during delithiation and lithiation of electrodes [9,12,41]. The differential voltage (DV) as a function of the electrode SOC is displayed in Fig. 3(c) for delithiation and in Fig. 3(d) for lithiation of the SiG. The DV is normalized by multiplying by the actual coin-cell capacity C_{act} during the (dis-)charge step.

During the (de-)lithiation of graphite, different crystallographic phases, so-called stages, form in the graphite [42–47]. The central peak G_5 in Fig. 3(c) is located at $\text{SOC} = 58.5\%$ for cell #1 (11 EFC)

Table 3

Mean standard deviation of the OCP of the coin-cells built from one electrode over the whole SOC range (σ_{OCP}) measured during the first and the second low-current CC charging and discharging step.

Electrode Full-cell #	SiG					NMC-811				
	N_{coin}	σ_{OCP} 1st ch./mV	σ_{OCP} 2nd ch./mV	σ_{OCP} 1st dch./mV	σ_{OCP} 2nd dch./mV	N_{coin}	σ_{OCP} 1st ch./mV	σ_{OCP} 2nd ch./mV	σ_{OCP} 1st dch./mV	σ_{OCP} 2nd dch./mV
1	5	2.7	2.9	3.0	3.5	6	2.3	1.7	2.8	3.0
2	6	3.1	2.5	1.7	0.8	6	2.5	5.4	4.9	9.8
3	6	3.2	2.9	4.4	3.5	6	5.7	13.8	9.4	54.5
5	4	2.5	1.9	3.4	3.0	3	4.0	13.4	9.2	52.3
6	4	1.8	3.5	0.6	3.6	4	8.7	2.5	9.1	8.6
7	6	1.9	2.7	2.7	3.3	5	2.2	2.7	7.5	9.9
8	6	2.3	3.1	3.0	3.4	6	1.1	1.0	2.2	2.0
Mean	5.3	2.5	2.8	2.7	3.0	5.1	3.8	5.8	6.4	20.0

and corresponds to graphite stage 2. This graphite stage corresponds to a lithiation degree of the graphite of 50% [42]. The fact that the peak is at a higher electrode SOC than 50 % is due to the fact that the silicon significantly contributes to the total electrode capacity but is not significantly delithiated in the SOC range above peak G_5 . The potential of silicon exhibits a steep increase right at the beginning of the delithiation and therefore significant lithium extraction from silicon only takes place at potentials higher than approximately 0.22 V [48,49]. The main voltage plateaus of graphite are at lower voltages [42,49] which has the effect that mainly graphite is delithiated until the cell potential reaches approximately 0.22 V [49]. Therefore, the charge extracted until graphite stage 2 is reached is mainly drawn from the graphite. Peak G_5 tends to appear at lower SOC with increasing number of full-cell cycles. This is probably due to a decrease in the relative contribution of the silicon to the overall electrode capacity during aging [28,48]. The peaks G_1 – G_4 correspond to lower lithiated graphite stages. Peak G_1 corresponds to graphite stage 4 which is expected at a graphite lithiation degree of 17% [41] while the corresponding peak appears at a higher electrode SOC because of the contribution of the silicon to the electrode capacity. Peak G_1 corresponds to a cell voltage of 0.211 V for the pristine anode samples. Therefore, significant delithiation of silicon should mainly take place below this peak. All peaks G_1 – G_4 exhibit a shift to lower SOC for aged cells. The reason for this shift is most probably the same as for the shift of peak G_5 , i.e., a reduced contribution from the silicon to the overall electrode capacity [28,48] which is accessed at low electrode SOC. Reduced silicon capacity is probably also the reason for the left-shift of the steep ascend to the left of the DV valley corresponding to the graphite voltage plateau (stage 4-1L phase transition) [44,49] around SOC = 15–20%. At low SOC there are local peaks corresponding to silicon phases. A detailed analysis of the progression of these peaks during aging is not possible because the curves shown in Fig. 3(c) appear to be blurred at SOC < 13% for the aged cells, which is probably due to the different delithiation behavior of the individual electrode samples in this SOC region, which is discussed later.

In addition to the DVA, the delithiation of the SiG samples is analyzed via incremental capacity analysis (ICA). Incremental capacity (IC) during delithiation, normalized by multiplying with the inverse of the actual capacity extracted during the delithiation step C_{act} , is plotted as a function of half-cell voltage (vs. Li/Li⁺) in Fig. 3(e). In this representation, the peaks correspond to voltage plateaus which indicate phase transitions. Peaks G_1 to G_{VI} correspond to phase transitions of the graphite [44]. In the voltage region up to 0.240 V, there are only minor differences between the curves obtained at different aging stages. Especially the main graphite transition peaks G_I around 0.098 V, G_{II} around 0.138 V, and G_{VI} around 0.225 V are approximately at the same voltages for different aging states. This indicates that the same graphite stages are formed during delithiation independent of electrode degradation.

There are up to three more peaks at higher potentials (S_I – S_{III}), which correspond to phase transitions during the delithiation of silicon [27,50–52]. The main change in the IC curves is that the normalized IC in the silicon-dominated voltage regime above 0.24 V generally

decreases with aging. This sign of a decrease in the relative capacity contribution of the silicon underlines the results from the DVA. The decrease in the relative contribution of silicon to the electrode capacity is estimated by the change in the capacity fraction accessed above 0.24 V during delithiation. A similar approach was presented by Klett et al. [48]. In Fig. 4 the fraction of the capacity accessed above 0.24 V during delithiation is shown for different aging stages. 0.24 V is above the highest graphite voltage plateau, therefore silicon delithiation should dominate the capacity accessed above this voltage. The fraction of the capacity accessed above 0.24 V decreases from 15.1% to 11.7% which is a decrease by 22.7%.

Contrary to this general trend, peaks S_{II} and S_{III} , which are at 0.37 V and 0.42 V, are more pronounced for some of the aged cells. Here, it has to be considered that there are significant differences between the individual coin-cells built from one electrode.

The individual SiG samples show significant differences in their voltage curves in the SOC region below approximately 15% during delithiation. As an example of the differences in delithiation curves, the voltage curves of the coin-cells built from cell #7 (446 EFC) are shown in Fig. 5(a). The voltage curves in Fig. 5(a) lie closely together for most parts of the delithiation, proving the high reproducibility of the measurement. Contrary to this, in the SOC region between 5% and 12%, there are comparably large differences between the coin-cell voltages reaching up to 38 mV. The shown example is representative for the finding that silicon-related features in the quasi-stationary OCP curves during delithiation in this SOC region are pronounced to different degrees for different samples. We interpret this as a sign of the inhomogeneity of the SiG electrode. This inhomogeneity is also the cause for the blurring of the DV curves in the low SOC region during delithiation shown in Fig. 3(c).

There are also qualitative differences between the delithiation IC curves of individual samples. The shape of the IC curve above 0.24 V can be divided into two categories referred to as ‘type A’ and ‘type B’ for the individual coin-cells. Representative curves are shown in Fig. 5(b). IC curves of type A have a distinct sharp peak around 0.27 V and a very broad peak between 0.40 V and 0.45 V. IC curves of type B exhibit three sharp peaks at 0.27 V, 0.37 V and 0.42 V respectively. In the literature, two IC peaks corresponding to phase transitions during delithiation of silicon have been reported: One around 0.27 V [27,51,52] and another one between 0.4 V and 0.5 V [27,51,52].

The fraction of coin-cells exhibiting an IC curve of type A decreases with aging, which is shown in Fig. 5(c). Correspondingly, the fraction of cells exhibiting IC curves of type B with sharp peaks at 0.37 V and 0.42 V increases. This results in an overall increase in height for the IC peaks S_{II} and S_{III} based on the averaged delithiation curves in Fig. 3(e).

To understand the processes occurring during the delithiation of silicon shown in Fig. 3(e) and to give a possible explanation for the increase of peak S_{III} , knowledge about the phase constitution of the lithiated silicon at the beginning of the delithiation is crucial. Most of the samples exhibit an IC peak below 0.05 V during the very first lithiation step directly after the coin-cell assembly, preceding the delithiation shown in Fig. 3(e). This is an indicator for the formation of crystalline c-Li₁₅Si₄ [50]. The fraction of working coin-cells at a certain aging stage

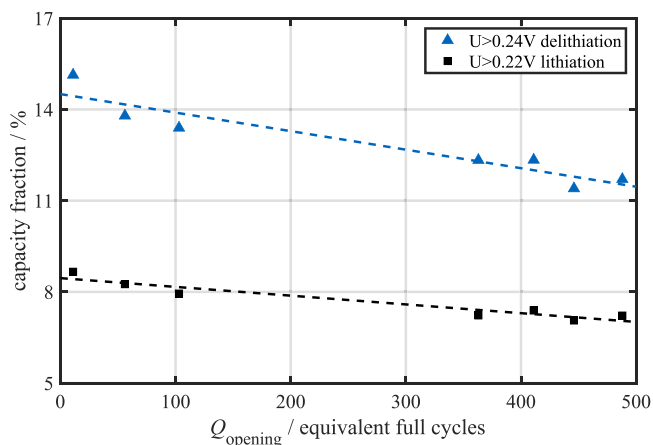


Fig. 4. Fraction of the capacity of silicon-graphite samples which is accessed above 0.24 V (vs. Li/Li⁺) during delithiation and above 0.22 V during lithiation based on averaged quasi-stationary (de-)lithiation curves measured for samples harvested from full-cells which have experienced a different total charge throughput before cell opening Q_{opening} .

exhibiting this peak is shown in Fig. 5(c). We therefore assume that most of the samples contain crystalline c-Li₁₅Si₄ at the beginning of the delithiation step shown in Fig. 3(e).

Following the model for the delithiation of c-Li₁₅Si₄ presented by Jiang et al. [53], amorphous a-Li_xSi is formed as an intermediate phase during the delithiation of c-Li₁₅Si₄. The fraction of a-Li_xSi formed as an intermediate phase is higher if more free surface of silicon is exposed, because the surface energy barrier of the electrochemical amorphization of c-Li₁₅Si₄ is lower [53]. The IC peak S_{III} in Fig. 3(e) can be associated with lithium extraction during the phase transition from a-Li_xSi to a-Si [51]. Therefore, the overall increase of peak S_{III} in Fig. 3(e) might possibly be linked to an increase in the relative amount of a-Li_xSi formed during the delithiation. This increase in the formation of a-Li_xSi might be caused by a morphological change of the silicon during aging resulting in an increase in active silicon surface [53]. Further research is necessary to explain the mechanisms leading to the change in silicon delithiation behavior.

The absolute difference between the mean delithiation OCP curve obtained from the pristine anode samples and the mean of the aged anode samples is shown in Fig. 3(g). The standard deviation between the single OCP curves used to calculate the average curve is shown as shaded areas. The decrease in OCP at SOC below approximately 15% SOC, between 18 and 40% SOC and between 52 and 65% SOC significantly exceeds the standard deviation between the samples taken from one electrode. The changes are probably due to the fact that the SOC where individual phase transitions are reached shifts to lower values due to the decrease in relative silicon capacity.

3.4. Change in the silicon-graphite lithiation open-circuit potential curve during cycle aging

The quasi-stationary OCP during lithiation of the anode samples is displayed in Fig. 3(b), the corresponding normalized DV is shown in Fig. 3(d). The features of the curve in Fig. 3(d) are similar to the features of the DV during delithiation: There are five peaks (G₁–G₅) corresponding to graphite phases. Peak G₅ corresponds to stage 2 while peaks G₁–G₄ correspond to graphite phases with lower lithiation degree. Peaks G₁–G₅ shift to lower SOC as cell aging progresses, which is probably due to the decrease in the silicon contribution to the electrode capacity [28,48]. In comparison to the DV curves during delithiation, the peaks exhibit a smaller left-shift for the lithiation case. The most probable reason for this is that the OCP of silicon shows a pronounced hysteresis and lies at lower potentials for the lithiation in

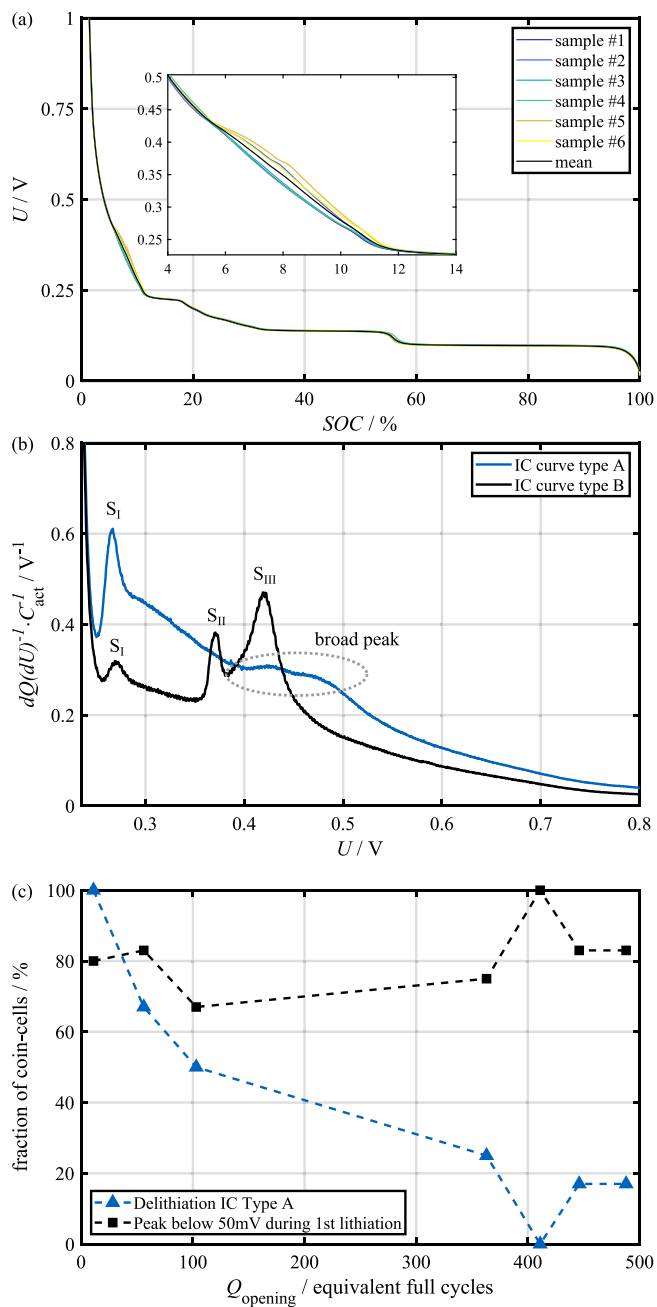


Fig. 5. (a) Voltage of silicon-graphite samples harvested from full-cell #7 (446 EFC) vs. Li/Li⁺ during quasi-stationary delithiation as a function of the SOC of the individual coin-cells. In addition to the voltage of the individual samples, the arithmetic mean retrieved at different SOC interpolation points is indicated. The inset shows an enlarged section of the SOC region where the curves obtained from different samples exhibit significant differences. (b) Normalized incremental capacity vs. cell voltage (vs. Li/Li⁺) during delithiation for two coin-cells containing silicon-graphite samples. The two samples exhibit the qualitatively different incremental capacity curves ‘type A’ (extracted from full-cell #1) and ‘type B’ (extracted from full-cell #7). (c) Fraction of silicon-graphite samples exhibiting an incremental capacity curve of type A during the first delithiation at different aging stages and fraction of silicon-graphite samples exhibiting an incremental capacity peak below 50 mV vs. Li/Li⁺ during the first lithiation after the coin-cell assembly at different aging stages.

comparison to the delithiation [54]. So even though a major part of the silicon capacity is lithiated at the beginning of the lithiation step [49], there should also be a significant fraction of the silicon capacity being lithiated in parallel with the graphite at potentials < 0.2 V. Still, most of the silicon capacity is probably accessed at potentials > 0.2 V [49] and therefore the left-shift of peaks G₁–G₅ can be attributed to the relative decrease in the silicon capacity.

Peaks S_1 and S_2 are associated with phases of silicon [8,37]. Both peaks exhibit a shift to lower SOC during aging, which can be explained by the decrease in relative silicon capacity. S_2 is only weakly pronounced. Still, these peaks appear much more clearly during lithiation than during delithiation for all aging stages because the curves obtained from the single samples differ less in this SOC region. The phenomenon of large differences in silicon features between the individual samples which is observed during delithiation is not as pronounced as during lithiation. A possible explanation for this is that the lithiation process might be more homogeneous than the delithiation process, possibly because graphite and silicon are lithiated to a greater extent in parallel than they get delithiated due to the large hysteresis of silicon [54]. There is an additional peak S_C in Fig. 3(d) which is not observable during delithiation. This peak probably corresponds to the highly lithiated, crystalline phase $c\text{-Li}_{15}\text{Si}_4$ which is formed during lithiation at potentials < 0.05 V vs. Li/Li^+ [50].

In Fig. 3(f) the phase transitions during lithiation are analyzed via ICA. The most pronounced peaks G_I – G_{VI} can be assigned to the graphite phase transitions, with the main graphite phase transitions occurring around 0.080 V (G_I), around 0.114 V (G_{II}), and around 0.204 V (G_{VI}) [49]. They do not exhibit clear trends in their height and position for the different aging stages, indicating that the graphite-related reactions stay the same during aging. Peak G_I exhibits comparably large deviations between the different aging stages, but without showing a specific trend. This is probably due to the comparably large difference between the single samples during lithiation at SOC $> 30\%$. There is a small peak observable between 0.28 V and 0.29 V which can be attributed to a silicon phase transition [50]. The silicon-induced IC peak around 0.1 V reported by some authors [50,52] is not visible, probably because it is superimposed with the graphite features. Around 0.026 V there is a distinct peak S_C which corresponds to the formation of crystalline lithiated silicon $c\text{-Li}_{15}\text{Si}_4$ [50]. Both silicon-related peaks decrease in height with progressing aging which is a sign of the decrease in the relative contribution of silicon to the overall electrode capacity. In addition to that, the level of normalized IC of the curves above 0.22 V, where most of the lithiation of the silicon occurs [49], is lower, indicating a reduced contribution of silicon to the electrode capacity. The fraction of the capacity accessed at potentials above 0.22 V during lithiation is indicated in Fig. 4 for different aging stages. As for the delithiation case, there is a significant decrease in the fraction of the capacity accessed at higher potentials. The fraction of the capacity accessed above 0.22 V decreases from 8.7% to 7.2% which is a decrease by 16.7%. Both the absolute numbers of the capacity fraction accessed in the chosen potential window and the relative decrease during aging are smaller than for the delithiation case. This is probably due to the fact that the lithiation of graphite and silicon occurs to a higher degree in parallel at lower potentials and a separation of the capacity contributions using this method is difficult.

In Fig. 3(h) the absolute difference in the averaged lithiation OCP curves between pristine and aged SiG samples is shown as solid lines and the standard deviation between the coin-cells as shaded areas. In between 5 and 30% SOC the average voltage is lower for aged cells because the phases of graphite and silicon are reached at lower electrode SOC due to the lower silicon capacity. Above 30% SOC both the standard deviation increases and the absolute of the voltage difference decreases. The trend towards lower voltages for aged cells visible below 30% SOC is not observed at higher SOC.

Our general finding of a lower OCP vs. electrode SOC for aged SiG anodes is consistent with the literature [29], and we conclude that the changes are due to a predominant degradation of silicon in comparison to graphite [28,29,48,54,55]. Possible degradation mechanisms of the silicon are the ionic and electric isolation of silicon particles [28,48,54] and change in the local structure, electrode morphology, and mechanical properties during cycling [28,54]. This does not mean that there is no degradation of the graphite, but the capacity provided by the silicon decreases at a higher rate than the capacity provided by the graphite.

The individual degradation rates of graphite and silicon most probably depend on the operating conditions used for the full-cell cycling. In this study, the cell is discharged to the lowest voltage recommended by the manufacturer, which probably enhances silicon utilization and therefore silicon degradation [54,56]. Such deep cycles only rarely occur in real-world applications. The change in anode OCP due to selective silicon degradation might therefore be smaller in applications compared to our results. On the other hand, the comparably high current rate during the cycling period could lead to a reduced silicon utilization [56] compared to the usually lower average current rates used for example in automotive applications. However, the influence of the current rate on selective silicon degradation is probably smaller than the influence of the voltage window.

Besides the change in graphite to silicon capacity ratio we do not observe the formation or disappearance of phases giving rise to a change in the shape of the OCP curve which is consistent with the literature [29]. The only exception are the subtle changes in silicon-related IC features during delithiation which need to be investigated in more detail in future studies.

3.5. Change in the cathode open-circuit potential curve during cycle aging

The average quasi-stationary OCP of the cells containing cathode samples at different aging stages is displayed in Fig. 6(a) for charging (delithiation of the NMC) and in Fig. 6(b) for discharging (lithiation of the NMC). The normalized DV during delithiation is shown in Fig. 6(c). The DV during delithiation exhibits three peaks indicating NMC phases [36] (C_1 – C_3). The exact position and height of the peaks show some variation for the different aging stages but there is no significant trend in position or height with the progress of aging. In Fig. 6(e) the normalized IC during delithiation is shown. The IC exhibits four peaks (C_I – C_{IV}) corresponding to phase transitions of the NMC at 3.56 V, 3.74 V, 4.01 V, and 4.18 V. No specific trend with aging can be observed for the height and position of the IC peaks.

The normalized DV during lithiation of the cathode samples shown in Fig. 6(d) exhibits three peaks (C_1 – C_3) similar to the delithiation case. Peak C_1 and the valley left to it exhibit a subtle shift towards lower SOC during aging while peak C_2 does not change with aging. Peak C_3 is very broad during lithiation which makes it difficult to detect aging-related trends. The most pronounced change during aging is the left-shift of the steep ascend towards the end of the lithiation process for aged cells in comparison with the less aged cells #1 and 2. Still, it has to be noted that the SOC position of the DV ascend does not follow an aging-related trend for cells #3–8. As for the delithiation case, the normalized IC during lithiation shown in Fig. 3(f) has four peaks. They are located at 3.54 V (C_I), 3.73 V (C_{II}), 4.00 V (C_{III}), and 4.17 V (C_{IV}). There are some differences between the curves of the less aged cells #1 and 2 and the other cells. The most prominent difference is that peak C_I is distinctively pronounced only for cells #1 and 2 while it is smeared out for the more aged cells. This feature corresponds to the left-shifted and less sharp decrease in voltage towards the end of the lithiation for the more aged cells shown in Fig. 6(b), which has also been reported in the literature [33]. Additionally, both slopes of peak C_{IV} are slightly left-shifted for cells #3–8 in comparison to cells #1 and 2. This corresponds to the faster decrease in voltage at the beginning of the lithiation depicted in Fig. 6(b). Apart from these subtle differences, there is no significant change in the overall shape of the lithiation IC curves during aging.

Our results show that the shape of the OCP curve of NMC-811 does not change significantly during cycle aging, even though the material most probably degrades. The formation of a resistive, electrochemically inactive layer on the surface of the primary particles [32,57,58], which leads to electrode capacity decrease [57] and severe increase in the charge transfer resistance [32,57], as well as cracking of secondary particles [29,32] has been reported to occur in nickel-rich NMC during prolonged cycling. Another aging mechanism is the formation of

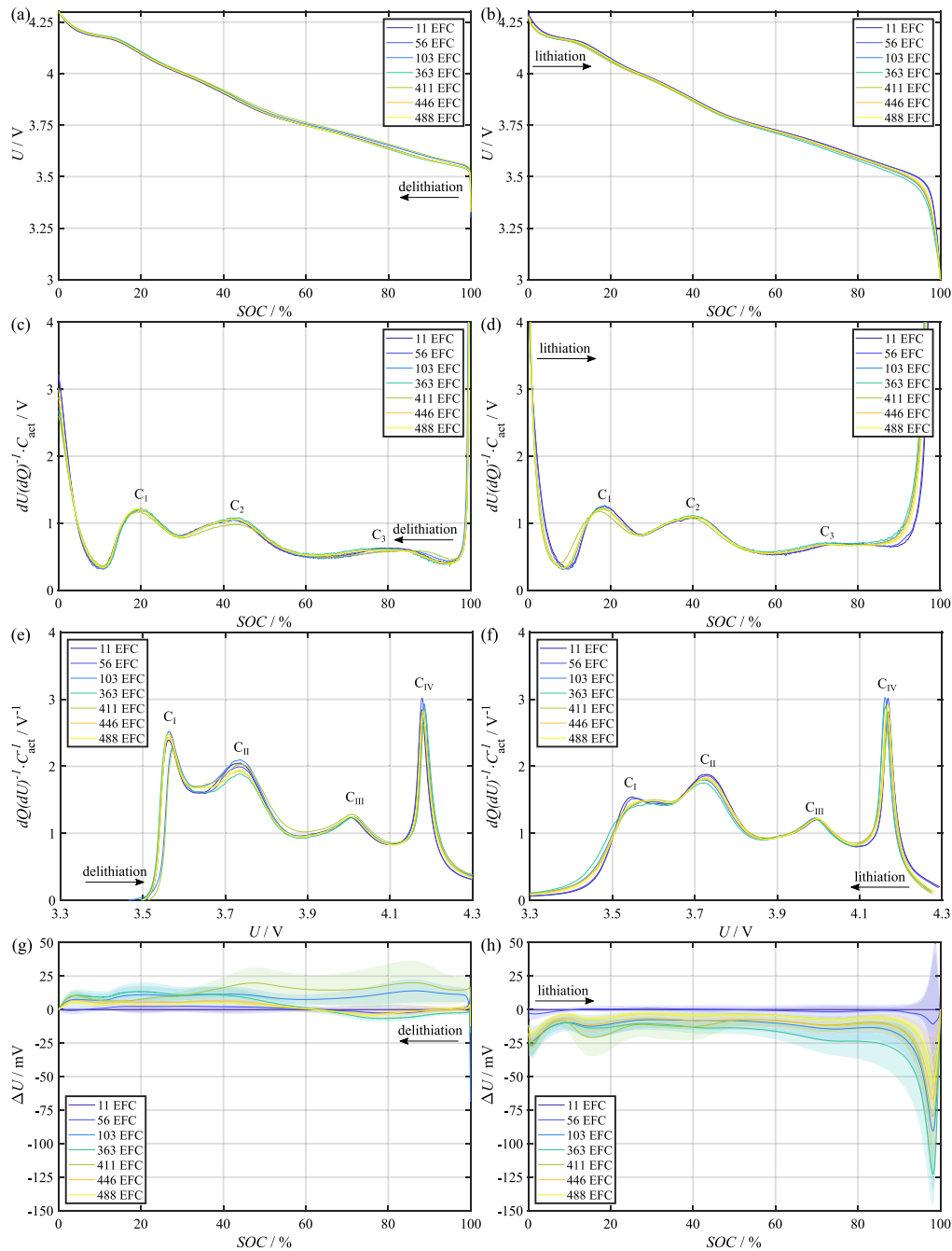


Fig. 6. First row: Mean quasi-stationary OCP vs. Li/Li^+ during (a) delithiation and (b) lithiation of the NMC samples extracted from full-cells that have been cycled for the number of equivalent full cycles indicated in the legend. Second row: Differential voltage during (c) delithiation and (d) lithiation of the NMC samples calculated based on the averaged OCP curves. The differential voltage values are normalized by multiplying with the actual capacity during the respective (dis-)charging step C_{act} and smoothed using a moving average filter. Third row: Incremental capacity during (e) delithiation and (f) lithiation of the NMC samples calculated based on the averaged OCP curves and plotted against cell voltage vs. Li/Li^+ . The incremental capacity values are normalized by multiplying with the inverse of the actual capacity during the respective (dis-)charging step C_{act} and smoothed using a moving average filter. Fourth row: Difference between mean OCP of aged NMC samples and mean OCP of pristine NMC samples during (g) delithiation and (h) lithiation. The standard deviation between the OCP of the single samples harvested from the same electrode is shown as shaded area.

a fatigued bulk phase, which can only be partly delithiated under regular cycling conditions due to kinetic limitations [32,58]. While these mechanisms probably also occur in the NMC electrodes in this study, we want to emphasize that the shape of the OCP curve is not significantly altered by them. This is in accordance with the literature. Jung et al. showed that the mean discharge voltage and the shape of the OCP curve of NMC-811 that was not exposed to ambient air does not significantly change during cycle aging [31]. Friedrich et al. showed that the charge-averaged mean discharge voltage of NMC-811 does not change significantly if a low current rate is used [57]. Former

studies investigating the cycle performance of commercial cells of the same type as the ones used in this study also do not report changes in the shape of the OCP curve of the cathode material [29,39,59]. There are some reports of a shift in the voltage position of the IC peaks of nickel-rich NMC during cycle aging, but the current rates used in these studies to obtain the IC curves are significantly higher than in our measurements [32,60], and it cannot be excluded that the shift in the voltage position of the peaks is due to an increase in the overpotential.

The invariance of the shape of the OCP curve suggests that the electrochemically active phases that are formed during delithiation and

lithiation do not change during cycle aging. This is in accordance with the literature as the bulk structure of NMC has been reported to stay the same during prolonged cycling [29,57,58]. The surface layer that is probably formed on the primary particles [57] does not affect the OCP curve as it is electrochemically inactive. We do not detect signs of an additional fatigued bulk phase towards the end of delithiation [32,58], but this does not mean that this phase does not exist. It has been reported that the fatigued phase can be almost completely delithiated during a prolonged CV phase giving enough time for the delithiation even though the kinetics are lower than for the pristine material [32]. As the quasi-stationary OCP is measured at a very low current rate of approximately C/90 in our experiments, the fatigued phase can probably be fully delithiated regardless of its low kinetics.

In Fig. 6(g) the difference between the mean quasi-stationary OCP during the delithiation of the aged cathode samples and the pristine cathode samples harvested from cell #1 is shown. The charge-averaged mean voltage during delithiation does not exhibit a clear trend with full-cell cycle aging and it is generally only slightly higher (< 14 mV) for the aged electrodes in comparison to pristine electrodes. The voltage difference during lithiation is presented in Fig. 6(h). The charge-averaged mean voltage during the lithiation of the aged samples is slightly lower (< 21 mV) in comparison to the pristine samples, even though there is no clear trend with aging. The subtle shift of the average voltage during delithiation and lithiation is probably due to an increase in the electrode impedance [29,32,57,61]. This increase in impedance probably leads to higher overpotentials even at the low current rate used for the measurement. An increase in electrode impedance is probably also the reason for the earlier and less sharp decrease in voltage towards the end of the lithiation [29].

Overall, we observe that there are no significant aging-induced changes in the shape of the OCP curve of the NMC-811, even though the material most probably degrades. For the development of model-based algorithms for SOH estimation, it is therefore appropriate to assume the shape of the half-cell OCP of NMC-811 to be invariant during cycle aging. The deviations of the absolute voltage vs. electrode SOC measured during low current (de-)lithiation are most probably due to an increase in electrode impedance. Such changes should therefore be considered by a change in the model elements or parameters describing the electrode impedance in a model describing the electrical behavior of an aged cell rather than by a change in the shape of the OCP curve.

4. Conclusion

We show that the shape of the OCP curve of silicon-graphite half-cells significantly changes during cycle aging of a full-cell containing these electrodes as anodes. Using DVA and ICA, we attribute these changes to a decrease in the relative contribution of the silicon to the electrode capacity. On the component level of this blended electrode, we observe a change in silicon-related features in the IC delithiation curve. Further research is necessary to understand the underlying mechanisms of this finding. In contrast to the changes in the SiG OCP curve, the shape of the OCP curve of NMC-811, which is used as cathode in the full-cells, exhibits only minor deviations as full-cell degradation progresses. This means that even though the NMC-811 probably degrades, it is appropriate to regard the shape of its OCP curve to be invariant in electrical cell models during cycle aging. The slight deviations between the quasi-stationary OCP curves of pristine and cycle aged cathode samples we observe are probably due to an increase in electrode impedance.

Another finding is that there are differences in the quasi-stationary OCP curve of individual coin-cells containing samples taken from nearby positions on the same electrode. We therefore use averaged OCP curves from several coin-cells for our analysis. Our recommendation for future studies using coin-cells containing harvested electrode samples is to build and measure several coin-cells containing material from the same electrode and use averaged measurement values in order to

reduce possible influences of the coin-cell manufacturing process and to obtain representative results for the whole electrode. Especially for the SiG during delithiation we find differences in the OCP curves of individual coin-cells, which are probably caused by inhomogeneity of the SiG electrode.

Our main conclusion is that in electrical battery models the shape of the OCP curve of NMC-811 can be regarded as fairly invariant during full-cell cycle aging while this does not apply to the shape of SiG half-cells. As anodes containing significant proportions of silicon are increasingly used in applications, it becomes more and more important to consider these changes in battery aging diagnostics and state estimation algorithms. While the results provided in this study concentrate on the aging-related changes on the half-cell OCP, we will investigate the impact of these changes on the full-cell OCP during aging in our future research. We will also investigate methods that make it possible to include the changes in half-cell OCP of blended SiG electrodes into electrical battery models.

CRedit authorship contribution statement

Julius Schmitt: Conceptualization, Methodology, Validation, Formal analysis, Investigation, Writing - original draft, Writing - review & editing, Visualization. **Markus Schindler:** Conceptualization, Methodology, Investigation, Writing - review & editing. **Andreas Jossen:** Writing - review & editing, Supervision, Project administration, Funding acquisition.

Declaration of competing interest

The authors declare that they have no known competing financial interests or personal relationships that could have appeared to influence the work reported in this paper.

Acknowledgments

This work was supported by the German Federal Ministry for Economic Affairs and Energy (grant number 03ETE019F) and by AUDI AG in the scope of an INITUM project. The responsibility for this publication lies with the authors.

References

- [1] S.F. Schuster, T. Bach, E. Fleder, J. Müller, M. Brand, G. Sxltl, A. Jossen, Nonlinear aging characteristics of lithium-ion cells under different operational conditions, *J. Energy Storage* 1 (2015) 44–53, <http://dx.doi.org/10.1016/j.est.2015.05.003>.
- [2] P. Keil, A. Jossen, Calendar aging of NCA lithium-ion batteries investigated by differential voltage analysis and coulomb tracking, *J. Electrochem. Soc.* 164 (1) (2016) A6066–A6074, <http://dx.doi.org/10.1149/2.0091701jes>.
- [3] P. Keil, S.F. Schuster, J. Wilhelm, J. Travi, A. Hauser, R.C. Karl, A. Jossen, Calendar aging of lithium-ion batteries, *J. Electrochem. Soc.* 163 (9) (2016) A1872–A1880, <http://dx.doi.org/10.1149/2.0411609jes>.
- [4] J. Schmitt, A. Maheshwari, M. Heck, S. Lux, M. Vetter, Impedance change and capacity fade of lithium nickel manganese cobalt oxide-based batteries during calendar aging, *J. Power Sources* 353 (2017) 183–194, <http://dx.doi.org/10.1016/j.jpowsour.2017.03.090>.
- [5] M. Naumann, M. Schimpe, P. Keil, H.C. Hesse, A. Jossen, Analysis and modeling of calendar aging of a commercial LiFePO₄/graphite cell, *J. Energy Storage* 17 (2018) 153–169, <http://dx.doi.org/10.1016/j.est.2018.01.019>.
- [6] A. Maheshwari, M. Heck, M. Santarelli, Cycle aging studies of lithium nickel manganese cobalt oxide-based batteries using electrochemical impedance spectroscopy, *Electrochim. Acta* 273 (2018) 335–348, <http://dx.doi.org/10.1016/j.electacta.2018.04.045>.
- [7] Y. Gao, J. Jiang, C. Zhang, W. Zhang, Y. Jiang, Aging mechanisms under different state-of-charge ranges and the multi-indicators system of state-of-health for lithium-ion battery with Li(NiMnCo)O₂ cathode, *J. Power Sources* 400 (2018) 641–651, <http://dx.doi.org/10.1016/j.jpowsour.2018.07.018>.
- [8] I. Zilberman, J. Sturm, A. Jossen, Reversible self-discharge and calendar aging of 18650 nickel-rich, silicon-graphite lithium-ion cells, *J. Power Sources* 425 (2019) 217–226, <http://dx.doi.org/10.1016/j.jpowsour.2019.03.109>.

- [9] J. Schmitt, B. Kraft, J.P. Schmidt, B. Meir, K. Elian, D. Ensling, G. Keser, A. Jossen, Measurement of gas pressure inside large-format prismatic lithium-ion cells during operation and cycle aging, *J. Power Sources* 478 (2020) 228661, <http://dx.doi.org/10.1016/j.jpowsour.2020.228661>.
- [10] P. Liu, J. Wang, J. Hicks-Garner, E. Sherman, S. Soukiazian, M. Verbrugge, H. Tataria, J. Musser, P. Finamore, Aging mechanisms of LiFePO₄ batteries deduced by electrochemical and structural analyses, *J. Electrochem. Soc.* 157 (4) (2010) A499, <http://dx.doi.org/10.1149/1.3294790>.
- [11] M. Dubarry, C. Truchot, B.Y. Liaw, Synthesize battery degradation modes via a diagnostic and prognostic model, *J. Power Sources* 219 (2012) 204–216, <http://dx.doi.org/10.1016/j.jpowsour.2012.07.016>.
- [12] I. Bloom, J.P. Christophersen, D.P. Abraham, K.L. Gering, Differential voltage analyses of high-power lithium-ion cells, *J. Power Sources* 157 (1) (2006) 537–542, <http://dx.doi.org/10.1016/j.jpowsour.2005.07.054>.
- [13] A. Marongiu, N. Nlandi, Y. Rong, D.U. Sauer, On-board capacity estimation of lithium iron phosphate batteries by means of half-cell curves, *J. Power Sources* 324 (2016) 158–169, <http://dx.doi.org/10.1016/j.jpowsour.2016.05.041>.
- [14] Z. Ma, Z. Wang, R. Xiong, J. Jiang, A mechanism identification model based state-of-health diagnosis of lithium-ion batteries for energy storage applications, *J. Clean. Prod.* 193 (2018) 379–390, <http://dx.doi.org/10.1016/j.jclepro.2018.05.074>.
- [15] I. Zilberman, S. Ludwig, M. Schiller, A. Jossen, Online aging determination in lithium-ion battery module with forced temperature gradient, *J. Energy Storage* 28 (2020) 101170, <http://dx.doi.org/10.1016/j.est.2019.101170>.
- [16] S. Wang, J. Wang, L. Vu, J. Purewal, S. Soukiazian, J. Graetz, On line battery capacity estimation based on half-cell open circuit voltages, *J. Electrochem. Soc.* 161 (12) (2014) A1788–A1793, <http://dx.doi.org/10.1149/2.0271412jes>.
- [17] S. Dey, Y. Shi, K. Smith, A. Colclasure, X. Li, From battery cell to electrodes: Real-time estimation of charge and health of individual battery electrodes, *IEEE Trans. Ind. Electron.* 67 (3) (2020) 2167–2175, <http://dx.doi.org/10.1109/TIE.2019.2907514>.
- [18] L. Ungurean, G. Cârstoiu, M.V. Micea, V. Groza, Battery state of health estimation: A structured review of models, methods and commercial devices, *Int. J. Energy Res.* 41 (2) (2017) 151–181, <http://dx.doi.org/10.1002/er.3598>.
- [19] Z. Li, J. Huang, B.Y. Liaw, J. Zhang, On state-of-charge determination for lithium-ion batteries, *J. Power Sources* 348 (2017) 281–301, <http://dx.doi.org/10.1016/j.jpowsour.2017.03.001>.
- [20] C. Campestrini, S. Kosch, A. Jossen, Influence of change in open circuit voltage on the state of charge estimation with an extended Kalman filter, *J. Energy Storage* 12 (2017) 149–156, <http://dx.doi.org/10.1016/j.est.2017.04.011>.
- [21] A. Marongiu, D. Sauer, On-board aging estimation using half-cell voltage curves for LiFePO₄ cathode-based lithium-ion battery for electric vehicle application, *World Electr. Veh. J.* 7 (1) (2015) 14–24, <http://dx.doi.org/10.3390/wevj7010014>.
- [22] S. Lee, J.B. Siegel, A.G. Stefanopoulou, J.-W. Lee, T.-K. Lee, Electrode state of health estimation for lithium ion batteries considering half-cell potential change due to aging, *J. Electrochem. Soc.* 167 (9) (2020) 090531, <http://dx.doi.org/10.1149/1945-7111/ab8c83>.
- [23] S. Lee, P. Mohtat, J.B. Siegel, A.G. Stefanopoulou, J.-W. Lee, T.-K. Lee, Estimation error bound of battery electrode parameters with limited data window, *IEEE Trans. Ind. Inf.* 16 (5) (2020) 3376–3386, <http://dx.doi.org/10.1109/TII.2019.2952066>.
- [24] C.R. Birkel, M.R. Roberts, E. McTurk, P.G. Bruce, D.A. Howey, Degradation diagnostics for lithium ion cells, *J. Power Sources* 341 (2017) 373–386, <http://dx.doi.org/10.1016/j.jpowsour.2016.12.011>.
- [25] I. Zilberman, J. Schmitt, S. Ludwig, M. Naumann, A. Jossen, Simulation of voltage imbalance in large lithium-ion battery packs influenced by cell-to-cell variations and balancing systems, *J. Energy Storage* 32 (2020) 101828, <http://dx.doi.org/10.1016/j.est.2020.101828>.
- [26] J.P. Schmidt, H.Y. Tran, J. Richter, E. Ivers-Tiffée, M. Wohlfahrt-Mehrens, Analysis and prediction of the open circuit potential of lithium-ion cells, *J. Power Sources* 239 (2013) 696–704, <http://dx.doi.org/10.1016/j.jpowsour.2012.11.101>.
- [27] M. Wetjen, D. Pritzl, R. Jung, S. Solchenbach, R. Ghadimi, H.A. Gasteiger, Differentiating the degradation phenomena in silicon-graphite electrodes for lithium-ion batteries, *J. Electrochem. Soc.* 164 (12) (2017) A2840–A2852, <http://dx.doi.org/10.1149/2.1921712jes>.
- [28] W.M. Dose, M.J. Piernas-Muñoz, V.A. Maroni, S.E. Trask, I. Bloom, C.S. Johnson, Capacity fade in high energy silicon-graphite electrodes for lithium-ion batteries, *Chem. Commun.* 54 (29) (2018) 3586–3589, <http://dx.doi.org/10.1039/c8cc00456k>.
- [29] X. Li, A.M. Colclasure, D.P. Finegan, D. Ren, Y. Shi, X. Feng, L. Cao, Y. Yang, K. Smith, Degradation mechanisms of high capacity 18650 cells containing Si-graphite anode and nickel-rich NMC cathode, *Electrochim. Acta* 297 (2019) 1109–1120, <http://dx.doi.org/10.1016/j.electacta.2018.11.194>.
- [30] D. Anseán, G. Baure, M. González, I. Cameán, A.B. García, M. Dubarry, Mechanistic investigation of silicon-graphite/LiNi_{0.8}Mn_{0.1}Co_{0.1}O₂ commercial cells for non-intrusive diagnosis and prognosis, *J. Power Sources* 459 (2020) 227882, <http://dx.doi.org/10.1016/j.jpowsour.2020.227882>.
- [31] R. Jung, R. Morasch, P. Karayaylali, K. Phillips, F. Maglia, C. Stinner, Y. Shao-Horn, H.A. Gasteiger, Effect of ambient storage on the degradation of Ni-rich positive electrode materials (NMC811) for Li-ion batteries, *J. Electrochem. Soc.* 165 (2) (2018) A132–A141, <http://dx.doi.org/10.1149/2.0401802jes>.
- [32] S. Schweidler, L. de Biasi, G. Garcia, A. Mazilkin, P. Hartmann, T. Brezesinski, J. Janek, Investigation into mechanical degradation and fatigue of high-Ni NCM cathode material: A long-term cycling study of full cells, *ACS Appl. Energy Mater.* 2 (10) (2019) 7375–7384, <http://dx.doi.org/10.1021/acsaem.9b01354>.
- [33] X. Jia, C. Zhang, Y. Le Wang, L. Zhang, W. Zhang, The degradation characteristics and mechanism of Li[Ni_{0.5}Co_{0.2}Mn_{0.3}]O₂ batteries at different temperatures and discharge current rates, *J. Electrochem. Soc.* 167 (2) (2020) 020503, <http://dx.doi.org/10.1149/1945-7111/ab61e9>.
- [34] F.M. Kindermann, A. Noel, S.V. Erhard, A. Jossen, Long-term equalization effects in Li-ion batteries due to local state of charge inhomogeneities and their impact on impedance measurements, *Electrochim. Acta* 185 (2015) 107–116, <http://dx.doi.org/10.1016/j.electacta.2015.10.108>.
- [35] J. Sieg, M. Storch, J. Fath, A. Nuhic, J. Bandlow, B. Spier, D.U. Sauer, Local degradation and differential voltage analysis of aged lithium-ion pouch cells, *J. Energy Storage* 30 (2020) 101582, <http://dx.doi.org/10.1016/j.est.2020.101582>.
- [36] J. Sturm, A. Rheinfeld, I. Zilberman, F.B. Spingler, S. Kosch, F. Frie, A. Jossen, Modeling and simulation of inhomogeneities in a 18650 nickel-rich, silicon-graphite lithium-ion cell during fast charging, *J. Power Sources* 412 (2019) 204–223, <http://dx.doi.org/10.1016/j.jpowsour.2018.11.043>.
- [37] M. Schindler, J. Sturm, S. Ludwig, J. Schmitt, A. Jossen, Evolution of initial cell-to-cell variations during a three-year production cycle, *eTransportation* 14 (165) (2021) 100102, <http://dx.doi.org/10.1016/j.etran.2020.100102>.
- [38] I. Zilberman, S. Ludwig, A. Jossen, Cell-to-cell variation of calendar aging and reversible self-discharge in 18650 nickel-rich, silicon-graphite lithium-ion cells, *J. Energy Storage* 26 (2019) 100900, <http://dx.doi.org/10.1016/j.est.2019.100900>.
- [39] M. Schindler, J. Sturm, S. Ludwig, A. Durdal, A. Jossen, Comprehensive analysis of the aging behavior of nickel-rich, silicon-graphite lithium-ion cells subject to varying temperature and charging profiles, *J. Electrochem. Soc.* (2021) <http://dx.doi.org/10.1149/1945-7111/ac03f6>.
- [40] A.U. Schmid, M. Kurka, K.P. Birke, Reproducibility of Li-ion cell reassembling processes and their influence on coin cell aging, *J. Energy Storage* 24 (2019) 100732, <http://dx.doi.org/10.1016/j.est.2019.04.006>.
- [41] D. Allart, M. Montaru, H. Gualous, Model of lithium intercalation into graphite by potentiometric analysis with equilibrium and entropy change curves of graphite electrode, *J. Electrochem. Soc.* 165 (2) (2018) A380–A387, <http://dx.doi.org/10.1149/2.1251802jes>.
- [42] J.R. Dahn, Phase diagram of LiC₆, *Phys. Rev. B* 44 (17) (1991) 9170–9177, <http://dx.doi.org/10.1103/PhysRevB.44.9170>.
- [43] D. Billaud, F.X. Henry, M. Lelaurain, P. Willmann, Revisited structures of dense and dilute stage II lithium-graphite intercalation compounds, *J. Phys. Chem. Solids* 57 (6–8) (1996) 775–781, [http://dx.doi.org/10.1016/0022-3697\(95\)00348-7](http://dx.doi.org/10.1016/0022-3697(95)00348-7).
- [44] T. Ohzuku, Y. Iwakoshi, K. Sawai, Formation of lithium-graphite intercalation compounds in nonaqueous electrolytes and their application as a negative electrode for a lithium ion (shuttlecock) cell, *J. Electrochem. Soc.* 140 (9) (1993) 2490–2498, <http://dx.doi.org/10.1149/1.2220849>.
- [45] D. Billaud, F.X. Henry, Structural studies of the stage III lithium-graphite intercalation compound, *Solid State Commun.* 124 (8) (2002) 299–304, [http://dx.doi.org/10.1016/S0038-1098\(02\)00469-6](http://dx.doi.org/10.1016/S0038-1098(02)00469-6).
- [46] S. Schweidler, L. de Biasi, A. Schiele, P. Hartmann, T. Brezesinski, J. Janek, Volume changes of graphite anodes revisited: A combined operando X-ray diffraction and in situ pressure analysis study, *J. Phys. Chem. C* 122 (16) (2018) 8829–8835, <http://dx.doi.org/10.1021/acs.jpcc.8b01873>.
- [47] M.P. Mercer, C. Peng, C. Soares, H.E. Hoster, D. Kramer, Voltage hysteresis during lithiation/delithiation of graphite associated with meta-stable carbon stackings, *J. Mater. Chem. A* 9 (1) (2021) 492–504, <http://dx.doi.org/10.1039/D0TA10403E>.
- [48] M. Klett, J.A. Gilbert, S.E. Trask, B.J. Polzin, A.N. Jansen, D.W. Dees, D.P. Abraham, Electrode behavior RE-visited: Monitoring potential windows, capacity loss, and impedance changes in Li_{1.03}(Ni_{0.5}Co_{0.2}Mn_{0.3}) 0.97 O₂/silicon-graphite full cells, *J. Electrochem. Soc.* 163 (6) (2016) A875–A887, <http://dx.doi.org/10.1149/2.0271606jes>.
- [49] M. Klett, J.A. Gilbert, K.Z. Pupek, S.E. Trask, D.P. Abraham, Layered oxide, graphite and silicon-graphite electrodes for lithium-ion cells: Effect of electrolyte composition and cycling windows, *J. Electrochem. Soc.* 164 (1) (2017) A6095–A6102, <http://dx.doi.org/10.1149/2.0131701jes>.
- [50] M.N. Obrovac, L. Christensen, Structural changes in silicon anodes during lithium insertion/extraction, *J. Power Sources* 7 (5) (2004) A93, <http://dx.doi.org/10.1149/1.1652421>.
- [51] J.W. Wang, Y. He, F. Fan, X.H. Liu, S. Xia, Y. Liu, C.T. Harris, H. Li, J.Y. Huang, S.X. Mao, T. Zhu, Two-phase electrochemical lithiation in amorphous silicon, *Nano Lett.* 13 (2) (2013) 709–715, <http://dx.doi.org/10.1021/nl304379k>.
- [52] A.Y.R. Prado, M.-T.F. Rodrigues, S.E. Trask, L. Shaw, D.P. Abraham, Electrochemical dilatometry of Si-bearing electrodes: Dimensional changes and experiment design, *J. Electrochem. Soc.* 167 (16) (2020) 160551, <http://dx.doi.org/10.1149/1945-7111/abd465>.

- [53] Y. Jiang, G. Offer, J. Jiang, M. Marinescu, H. Wang, Voltage hysteresis model for silicon electrodes for lithium ion batteries, including multi-step phase transformations, crystallization and amorphization, *J. Electrochem. Soc.* 167 (13) (2020) 130533, <http://dx.doi.org/10.1149/1945-7111/abbbba>.
- [54] M. Wetjen, S. Solchenbach, D. Pritzl, J. Hou, V. Tileli, H.A. Gasteiger, Morphological changes of silicon nanoparticles and the influence of cutoff potentials in silicon-graphite electrodes, *J. Electrochem. Soc.* 165 (7) (2018) A1503–A1514, <http://dx.doi.org/10.1149/2.1261807jes>.
- [55] M.-T.F. Rodrigues, J.A. Gilbert, K. Kalaga, D.P. Abraham, Insights on the cycling behavior of a highly-prelithiated silicon-graphite electrode in lithium-ion cells, *J. Phys. Energy* 2 (2) (2020) 024002, <http://dx.doi.org/10.1088/2515-7655/ab6b3a>.
- [56] P.-F. Lory, B. Mathieu, S. Genies, Y. Reynier, A. Boulineau, W. Hong, M. Chandesris, Probing silicon lithiation in silicon-carbon blended anodes with a multi-scale porous electrode model, *J. Electrochem. Soc.* 167 (12) (2020) 120506, <http://dx.doi.org/10.1149/1945-7111/abaa69>.
- [57] F. Friedrich, B. Strehle, A.T.S. Freiberg, K. Kleiner, S.J. Day, C. Erk, M. Piana, H.A. Gasteiger, Editors' choice—Capacity fading mechanisms of NCM-811 cathodes in lithium-ion batteries studied by X-ray diffraction and other diagnostics, *J. Electrochem. Soc.* 166 (15) (2019) A3760–A3774, <http://dx.doi.org/10.1149/2.0821915jes>.
- [58] C. Xu, K. Märker, J. Lee, A. Mahadevegowda, P.J. Reeves, S.J. Day, M.F. Groh, S.P. Emge, C. Ducati, B. Layla Mehdi, C.C. Tang, C.P. Grey, Bulk fatigue induced by surface reconstruction in layered Ni-rich cathodes for Li-ion batteries, *Nature Mater.* 20 (1) (2021) 84–92, <http://dx.doi.org/10.1038/s41563-020-0767-8>.
- [59] T.M.M. Heenan, A. Jnawali, M.D.R. Kok, T.G. Tranter, C. Tan, A. Dimitrijevic, R. Jervis, D.J.L. Brett, P.R. Shearing, An advanced microstructural and electrochemical datasheet on 18650 Li-ion batteries with nickel-rich NMC811 cathodes and graphite-silicon anodes, *J. Electrochem. Soc.* 167 (14) (2020) 140530, <http://dx.doi.org/10.1149/1945-7111/abc4c1>.
- [60] S.S. Zhang, Understanding of performance degradation of $\text{LiNi}_{0.80}\text{Co}_{0.10}\text{Mn}_{0.10}\text{O}_2$ cathode material operating at high potentials, *J. Energy Chem.* 41 (2020) 135–141, <http://dx.doi.org/10.1016/j.jechem.2019.05.013>.
- [61] K. Kleiner, P. Jakes, S. Scharner, V. Liebau, H. Ehrenberg, Changes of the balancing between anode and cathode due to fatigue in commercial lithium-ion cells, *J. Power Sources* 317 (2016) 25–34, <http://dx.doi.org/10.1016/j.jpowsour.2016.03.049>.